

Comparative *in-silico* study of drug release from intraocular implants for glaucoma treatment

Umar Pitafi¹, Tao Chen¹, Cynthia Yu-Wai-Man², Daniel Sebastia-Saez¹

¹School of Chemistry and Chemical Engineering, University of Surrey, Guildford, GU2 7XH, UK

²Faculty of Life Sciences & Medicine, King's College London, London, SE1 1UL, UK

Keywords

Computational Fluid Dynamics; glaucoma; intraocular pressure; ocular drug-releasing implant; drug delivery

Corresponding Authors:

Cynthia Yu-Wai-Man, King's College London, cynthia.yu-wai-man@kcl.ac.uk

Daniel Sebastia-Saez, University of Surrey, j.sebastiasaez@surrey.ac.uk

List of symbols

Latin symbols

c – Concentration; $\text{mol}\cdot\text{m}^{-3}$

c_{un} – Concentration of undissolved species ; $\text{mol}\cdot\text{m}^{-3}$

D – Diffusion coefficient ; $\text{m}^2\cdot\text{s}^{-1}$

\vec{g} – Acceleration due to gravity; $\text{m}\cdot\text{s}^{-2}$

h_C, h_i, h_{il} – Height of anterior chamber, iris and iris-lens channel respectively; mm

I – Identity matrix

\vec{J} – Molar flux; $\text{mol}\cdot\text{m}^{-2}\cdot\text{s}^{-1}$

k_b – Boltzmann constant; $\text{J}\cdot\text{K}^{-1}$

L_{TM} – Length of the trabecular meshwork; mm

MW – Molecular weight; Da

p – Pressure; Pa

r – Molecular radius; Å

R_C, R_L, R_p – Radius of posterior cornea, lens and pupil, respectively; mm

T – Temperature; K

\vec{u} – Velocity; $\text{m}\cdot\text{s}^{-1}$

Greek symbols

β – Drug delivery rate; $\text{m}^2\cdot\text{s}^{-1}\cdot\text{mol}^{-2/3}$

ε – porosity; dimensionless

κ – Permeability

μ – Dynamic viscosity; $\text{Pa}\cdot\text{s}$

ρ – Density; $\text{kg}\cdot\text{m}^{-3}$

Other symbols

∇ – Nabla operator

List of abbreviations

AC – Anterior chamber

AH – Aqueous humour

ALT – Argon laser trabeculoplasty

AS – Anterior segment

CFD – Computational Fluid Dynamics

ECM – Extracellular matrix

FEM – Finite Element Method

IOL – Intraocular lens

IOP – Intraocular Pressure

PC – Posterior chamber

PLGA – poly(lactic-*co*-glycolic) acid

SLT – Selective laser trabeculoplasty

TM – Trabecular meshwork

Abstract

Drug-releasing implants are gaining momentum in the treatment of glaucoma. However, they present several limitations, such as the inability to provide an even distribution of the drug in the trabecular meshwork. CFD simulations were used in this work to study the interplay between ocular fluid dynamics and drug diffusion to explore the options to achieve a homogeneous drug distribution in the target tissue. The analysis finds that thermal convective currents do not result in efficient mixing within the eye's anterior chamber. This results in highly localized drug delivery in the trabecular meshwork when using a gravity-placed cylindrical implant. Placing the implant in the posterior chamber results in improved mixing, although it presents the risk of therapeutical drugs being absorbed by the corneal endothelium instead of reaching the trabecular meshwork. Finally, a ring implant next to the trabecular meshwork is tested, which would give rise to a homogeneous concentration around the entirety of the trabecular meshwork. However, implanting a 360° ring with cylindrical cross-section next to the trabecular meshwork can entail significant surgical challenges, so the solution could consist of smaller cylindrical ring segments to attain a sufficient aqueous humour draining rate for each specific patient.

1. Introduction

Glaucoma is a chronic, progressive optic neuropathy affecting around 70 million people worldwide ¹. This condition is characterised by elevated intraocular pressure (IOP), which results from increased resistance to the outflow of aqueous humour (AH). Glaucoma causes irreversible damage to the optic nerve and ultimately blindness ². Figure 1 shows a schematic of the eye's anterior segment (AS). The latter comprises the anterior chamber (AC), i.e., the space between the cornea and the iris, and the posterior chamber (PC). The conventional outflow pathway of the AH is represented by the blue arrow. The AH is produced in the ciliary body at a rate between 1.5 $\mu\text{l}/\text{min}$ and 3 $\mu\text{l}/\text{min}$ ³. From there, the fluid flows through the gap between the iris and the lens into the anterior chamber (AC) of the eye. It then reaches the trabecular meshwork (TM), where it is absorbed into the systemic circulation through the collector channels in the Schlemm's canal. The conventional outflow pathway is responsible for the evacuation of between 80 and 90% of the AH, with the alternative route being the uveoscleral pathway ^{4,5}, where the AH diffuses through the intercellular spaces of the ciliary body and is responsible for the drainage of the remaining AH. The uveoscleral pathway has not been considered in this study.

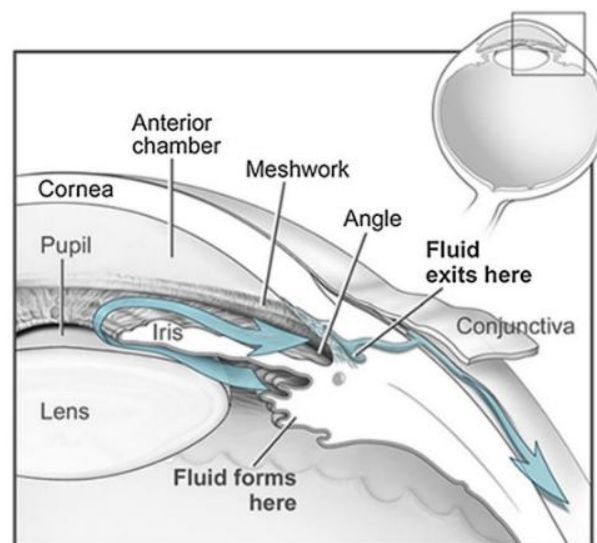


Figure 1 Schematic illustration of aqueous humour flow within the eye's anterior segment. Image reproduced with permission from ⁶

Glaucomatous conditions can develop in two ways, including open-angle glaucoma and closed-angle glaucoma. In open-angle glaucoma, which is the most common type of glaucoma, the TM loses its capacity to evacuate the AH due to fibrosis ⁷. The TM consists of an extracellular matrix (ECM), which is formed of collagen, fibronectin, fibrillin and hyaluronic acid, and is filled with trabecular meshwork cells. Fibrosis, which is the excessive deposition of the ECM

components in the TM leads to a reduced evacuation capability of the AH, hence resulting in increased IOP⁸. Under normal physiological conditions, IOP ranges between 10–21 mmHg. The risk of developing glaucoma increases significantly with IOP readings exceeding 21 mmHg. Closed-angle glaucoma is less common than open-angle glaucoma and is characterised by an abnormally narrow iridocorneal angle, which results in increased resistance of AH outflow. The simulations included in this study reproduce an open-angle glaucoma scenario.

The most common way to treat glaucoma focus on regulating IOP using eye drops to reduce the production rate of AH and/or outflow resistance⁹. Another treatment option is laser trabeculoplasty, which includes Selective Laser Trabeculoplasty (SLT) and Argon Laser Trabeculoplasty (ALT). These methods target the tissue of the TM to facilitate drainage. Invasive surgical interventions, like trabeculectomy and tube surgery, may become necessary in advanced glaucoma cases, but can lead to complications, such as cataract formation, hypotony and endophthalmitis¹⁰. In the case of closed-angle glaucoma, other forms of laser therapies exist, including laser iridotomy and iridoplasty.

The effectiveness of treatments based on eye drops relies heavily on patients' adherence, which is generally poor¹¹. The optimal treatment would provide a sustained drug release over time without having to rely on patient adherence. Given the limitations of topical treatments and surgery, the use of drug reservoirs, such as punctal plugs and external ocular inserts, is gaining popularity^{12,13}.

Durysta[®] and iStent iDose are the two implants currently approved by the FDA and available commercially^{14,15}. Durysta[®] is placed in the lower part of the iridocorneal angle, at the entry to the TM. With its standard cylindrical dimensions (i.e. 0.2 mm diameter and 1 mm length), one of the concerns with the use of Durysta[®] is the difficulty to achieve a homogeneous concentration of the released drug across the TM. This is because Durysta[®], given its small dimensions, functions as a point-source depot, and therefore delivers markedly higher drug concentrations to tissues adjacent to the implant than in distant tissues, where very low or undetectable levels would be delivered. Evidence of this is given in¹⁶, where the authors show that a bimatoprost implant (Bimatoprost SR) selectively delivered the drug into a specific tissue while low or undetectable concentrations were observed in surrounding tissues, as opposed to topical delivery.

While the location of Durysta[®] in the AC is driven by gravity, there are other placement solutions being developed. For instance, the travoprost implant iDose[®] TR uses a trabecular

anchor^{17,18}. Furthermore, another method under clinical trial at present is based on attaching a ring-shaped drug reservoir on the haptic legs of intraocular lenses (IOL) used in cataract surgery (<https://www.spyglasspharma.com>). Better drug mixing is expected when placing the implant in the PC than in the AC.

Understanding the interplay between ocular fluid dynamics and mass transport is key to accelerate the development of effective IOP-reducing, drug-releasing ocular implants. Mathematical simulations (i.e., *in-silico* methods) are gaining momentum as some authors highlight the small size of the AC and the implant as a limitation to carry out their experimental studies¹⁹. The use of animal models also presents ethical issues. Furthermore, *in-silico* methods can contribute to test different implant-location and size scenarios efficiently, hence suggesting further ways of drug delivery improvement.

There is a growing number of studies that deal with simulations of drug diffusion within the eye using Computational Fluid Dynamics (CFD)²⁰. A particularly relevant study is reported in²¹, where the authors varied implant parameters to study drug distribution focusing on an implant located in the haptic legs of an IOL. The authors concluded that effective diffusivity of the drug in the implant and the initial drug dosage were key to modulate drug delivery. They also stated that the shape of the implant can affect drug delivery. Here, we aim at studying the effect of shape and implant location on drug delivery. We show using 3-D CFD simulations, that current commercial solutions do give rise to heterogeneous drug distributions as suggested by experimental data¹⁶, and propose a new implant design to reduce the point source delivery effect of Durysta®. These findings may carry clinical significance, indicating that the geometric and positional constraints of existing implants could contribute to uneven therapeutic dosing of the trabecular meshwork and may therefore influence treatment efficacy.

2. Methodology

The simulations were carried out using the commercial FEM software COMSOL Multiphysics v6.3. The model represents a 3-D geometry of the human eye's anterior segment (AS) to analyze AH flow, heat transfer and drug release and transport from the porous intraocular implant. The geometric parameters are summarized in Table 1 while Figure 2 shows a schematic of the computational domain with mesh detail.

Table 1 Geometry parameters of the anterior segment.

Parameter	Value [mm]
Radius of posterior cornea ⁶	6.80
Maximum height of anterior segment ⁶	2.63
Lens radius ⁶	10.00
Height of iris-lens channel ^{6,22,23}	0.093
Iris thickness ²⁴	0.40
Pupil radius ²³	1.75

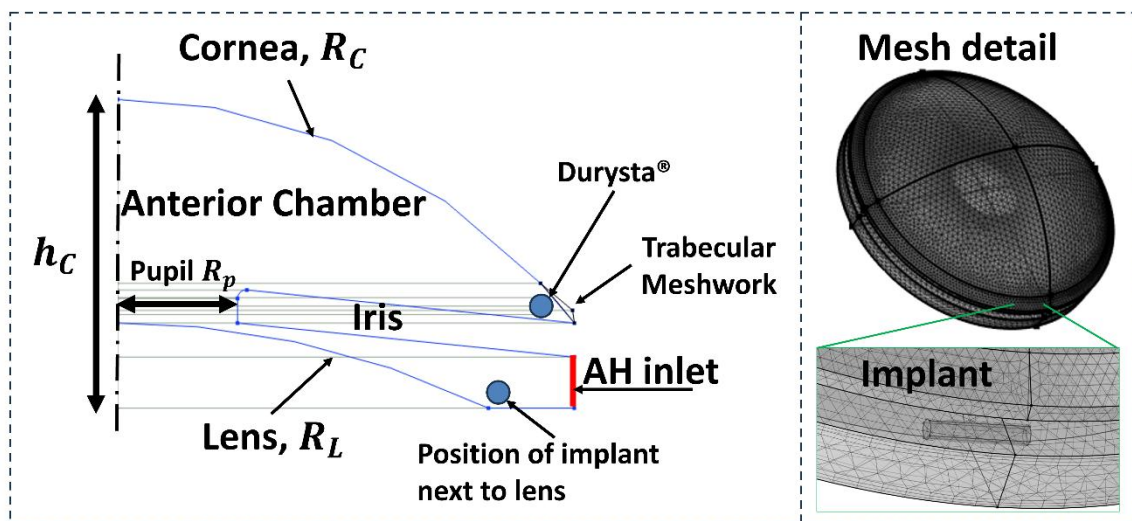


Figure 2 Schematic of the calculation domain. The geometry of the anterior segment was reproduced in 2-D and revolved around the symmetry axis. Then, a cylinder mimicking the implant was included in the geometry before meshing.

The implant was represented as a cylindrical porous medium with a diameter of 0.2mm and a length of 1 mm (i.e., the dimensions of Durysta[®]) placed in either (i) at the iridocorneal angle or (ii) at the vicinity of the IOL in the posterior chamber. This allowed a comparison of concentration profiles depending on the implant location. The simulations were run in two steps for computational economy reasons: the first step (static) solved the laminar flow of AH

coupled with heat transfer, the second step (dynamic) solved drug delivery from implant and transport of diluted species.

2.1 Fluid Dynamics

AH flow was modelled as an incompressible, Newtonian, single phase laminar flow during the first (static) step of the simulation. The flow field was computed using the laminar flow physics interface in COMSOL Multiphysics v6.3, solving the steady state Navier-Stokes equations. It is suggested in the literature that AH flow remains laminar even under the effect of saccadic movements^{25,26}. Other reported work suggested that liquified vitreous might experience short transitions to inertial effects being more significant than viscous effects under the effect of saccades, but do not support that turbulent flow might develop. No turbulent transition has been described in this model. considered as a drug mixing mechanism in this work. Saccades have not been considered either. The conservation of momentum equation is:

$$\rho(\mathbf{u} \cdot \nabla)\mathbf{u} = \nabla \cdot [-p\mathbf{I} + \mathbf{K}] + \mathbf{F} + \rho\mathbf{g} \quad (1)$$

And the conservation of mass:

$$\rho \nabla \cdot \mathbf{u} = 0 \quad (2)$$

Where ρ represents the density, \mathbf{u} is the velocity vector, \mathbf{K} represents the viscosity forces acting on the fluid, p is the pressure, \mathbf{I} is the identity matrix, and \mathbf{g} is the acceleration due to gravity. \mathbf{F} is the thermally-driven buoyant force, which can be defined using Boussinesq approximation. The trabecular meshwork and the implant were represented as porous subdomains, where the local momentum balance was modified according to Darcy's law.

A typical value for the porosity of a PLGA scaffold is 0.9²⁷. However, some sources describe Durysta[®] as a solid polymer implant^{28,29}, which suggests a low porosity. The implant was assigned a porosity of 0.5. The TM is divided in different zones that present varying degrees of porosity. A value of 0.6 was used in this model³⁰. However, little effect on flow patterns and velocity field results was observed when varying the porosity of both the TM and the implant. The size and shape parameters of the trabecular meshwork were obtained from³¹.

A no-slip boundary condition was implemented in the cornea, lens, iris, and haptic legs of the implant. An outlet boundary condition was set on the TM. A uniform inflow velocity of $v_0 = 2.03 \mu\text{m}\cdot\text{s}^{-1}$ was imposed at the AH inlet, corresponding to a physiological AH production rate of approximately $2.5 \mu\text{l}/\text{min}$ ³². A static intraocular pressure of 27 mmHg was applied to

represent glaucomatous conditions ⁶. Gravitational acceleration was included to assess the effect of body orientation (i.e., standing or supine) on AH flow.

2.2 Heat Transfer

The effect of heat transfer on AH flow was also calculated in the first step (static) of the simulations. To capture the thermally driven convective flow of AH, the heat transfer formulation employed in this study can be directly related to Pennes' Bioheat equation, which in its general form is expressed as:

$$\rho c_p \frac{\partial T}{\partial t} = \nabla \cdot (k \nabla T) + \rho_b c_b \omega_b (T_a - T) + Q_{met} + Q_{ext} \quad (3)$$

Where the additional terms $\rho_b c_b \omega_b (T_a - T)$ and Q_{met} account for blood perfusion and metabolic heat generation within biological tissues. In the case of AH, these effects are negligible because the fluid is avascular and has no metabolic activity. Furthermore, the simulations were conducted under steady state conditions allowing the transient term $\frac{\partial T}{\partial t}$ to be omitted. The symbols ρ , c_p and k are the density, specific heat capacity and thermal conductivity of AH, respectively.

Imposed boundary conditions were defined following the methodology in ³³. At the corneal surface, heat loss to the surrounding environment was modelled as a combination of convective, radiative and evaporative effects expressed as

$$-n \cdot q = q_{conv} + q_{rad} + q_{evap} \quad (4)$$

Where n is the unit outward normal vector and q is the conductive heat flux vector. The individual fluxes were specified as separate boundary conditions in COMSOL Multiphysics v6.3 as

$$q_{conv} = h_{amb}(T_{ext} - T) \quad (5)$$

And

$$q_{rad} = \epsilon \sigma (T_{ext}^4 - T^4) \quad (6)$$

Where h_{amb} is the ambient convective heat transfer coefficient, T_{ext} is the external air temperature, ϵ is the corneal emissivity and σ is the Stefan Boltzmann constant. A constant evaporative heat flux at the corneal surface, q_{evap} was assigned a constant value of 40 W/m²

to average heat loss due to tear-film evaporation under physiological conditions. A summary of parameters is included in Table 2.

A heat flux boundary condition (i.e., *blood convection*³³) was set on the rest of the solid boundaries including the iris and the lens.

Table 2 Numerical values of the parameters used in the eye's thermal boundary conditions³³.

Parameter	Description	Value
q_{evap}	Evaporation rate $W\ m^{-2}$	40
ε	Emissivity	0.975
h_{bl}	Blood convection coefficient $W\ m^{-2}\ K^{-1}$	65
h_{amb}	Ambient convection coefficient $W\ m^{-2}\ K^{-1}$	10
T_{ext}	External Temperature K	298
T_{bl}	Blood Temperature K	310

2.3. Mass transport

The steady-state thermal convective flow calculated in the first step (static) of the simulation was used as the initial condition to solve the transient mass transport of diluted species equation in the second step of the simulations coupled with the drug delivery kinetics from the implant. A dynamic study using a finite dose was chosen since Durysta® releases bimatoprost over the course of up to 15 weeks. Durysta® implements a dose of 10 μg of bimatoprost. The implant has a cylindrical shape with 0.2 mm of diameter and 1 mm height. This yields an initial concentration of 768 $mol \cdot m^{-3}$. The mass transport equation is:

$$\frac{\partial c}{\partial t} + \nabla \cdot \mathbf{J} + \mathbf{u} \cdot \nabla c = R \quad (7)$$

Where c is the concentration of bimatoprost and $\mathbf{J} = -D\nabla c$ accounts for Fick's diffusion flux. The source term $R = \beta c_{un}$ accounts in this case for the delivery of the undissolved drug from the implant and into the fluid flow of AH. The diffusion coefficient in water was calculated using the well-known Stokes-Einstein equation:

$$D = \frac{k_b T}{6\pi\mu r} \quad (8)$$

Where $T = 37^\circ\text{C}$ is the temperature of the eye and $\mu = 0.7269 \text{ mPa}\cdot\text{s}$ is the dynamic viscosity of water at that temperature. The parameter $k_b = 1.380649 \times 10^{-23} \text{ J/K}$ is the Boltzmann constant. The molecular radius r was calculated using the empirical expression:

$$r = \sqrt[3]{\frac{3}{4\pi} \times 0.9087 \times MW} \quad (9)$$

Which assumes spherical symmetry of the bimatoprost molecule.

2.4. Drug release kinetics

Bimatoprost presents a low solubility in the AH, therefore, it is not readily available in the implant for dissolution. Instead, hydrolysis and metabolic processes take place during the implant's biodegradation, which result in the drug being available for dissolution within the AH flow²⁸. Delivery from the implant has thus been implemented using the following equation and solved during the second (transient) step of the simulation:

$$\frac{\partial c_{un}}{\partial t} = -\beta c_{un} \quad (10)$$

Where c_{un} is the concentration of undissolved drug in the implant and β is the delivery rate that needs calibration as it is not readily available from experimental data in the literature. Similar qualitative results with different values of the calibrated constant β were obtained using the dissolution model presented by³⁴ and defined by the equation:

$$\frac{\partial c_{un}}{\partial t} = -\beta c_{un}^{\frac{2}{3}} (S - c) \quad (11)$$

Where S is the solubility of the drug in AH (water) and c is the concentration of the dissolved drug.

3. Results and discussion

3.1. Model verification and validation

Experimental flow field visualisation of AH in the eye presents obvious challenges that affect the availability of data for mathematical model validation. Model validation was carried out by comparing the simulated AH flow obtained with this model with previously reported models. The present model reproduced the thermal convective currents described in ^{33,35}, where the observed flow patterns were attributed to temperature-induced density differences between the cornea and iris. Differences were observed depending on body position. Figure 3 and Figure 4 report the comparison of AH flow patterns for the standing and supine body positions respectively. A central eddy in front of the pupil was observed in the standing position, while a symmetric arrangement of two eddies was observed in the supine position. Larger values of the AH velocity were observed in the standing position than in the supine position in the area next to the pupil. A maximum velocity of $1.03 \times 10^{-4} \text{ m}\cdot\text{s}^{-1}$ ($103 \text{ }\mu\text{m}\cdot\text{s}^{-1}$) was observed in ³³ for the standing position, while this work yielded $\approx 1.60 \times 10^{-4} \text{ m}\cdot\text{s}^{-1}$ ($160 \text{ }\mu\text{m}\cdot\text{s}^{-1}$). For the supine position, the maximum velocity observed in ³³ was $2.78 \times 10^{-5} \text{ m}\cdot\text{s}^{-1}$ ($27.8 \text{ }\mu\text{m}\cdot\text{s}^{-1}$), while this work yielded $\approx 30 \text{ }\mu\text{m}\cdot\text{s}^{-1}$) showing close agreement in both flow magnitude and pattern of convective currents and reflecting plausible biological variability.

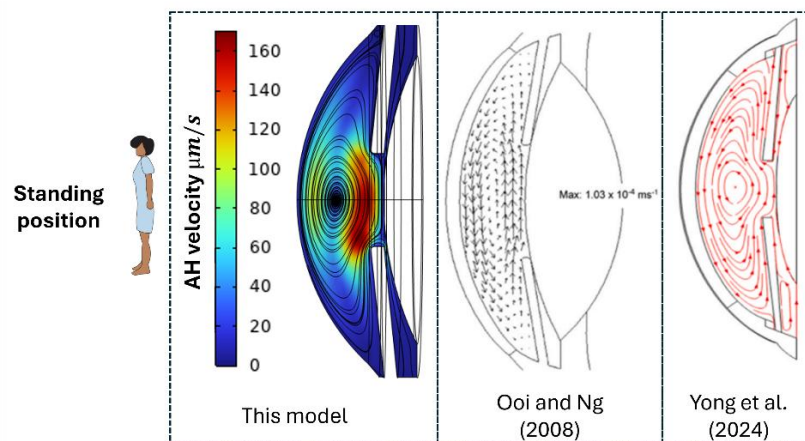


Figure 3 Comparison between the fluid flow patterns obtained with this model and those reported by Ooi et al. ³³ and Yong et al. ³⁵ for the standing position.

We also performed a grid independence test using the *fine*, *finer* and *extremely fine* settings in COMSOL Multiphysics v6.3, with differences in the results of less than 2% with respect to the *fine* mesh for the maximum velocity in all cases.

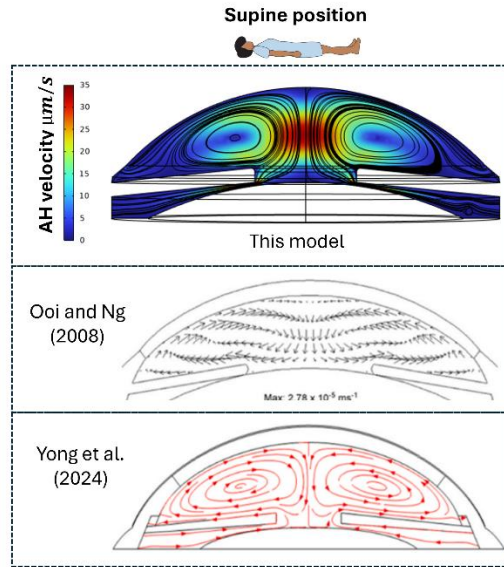


Figure 4 Comparison between the fluid flow patterns obtained with this model and those reported by Ooi et al.³³ and Yong et al.³⁵ for the standing position.

3.2. Calibration of drug releasing rate (β) from implant.

Calibration of the drug release rate β in eqn (10) was performed due to lack of available experimental data on the combined effect of hydrolysis and metabolism that leads to the release of bimatoprost from Durysta[®] into the AH. Figure 5 shows the temporal evolution of the amount of drug (normalised by initial dosage of 10 μg) remaining in the implant during the simulated 12 weeks' delivery for different values of β .

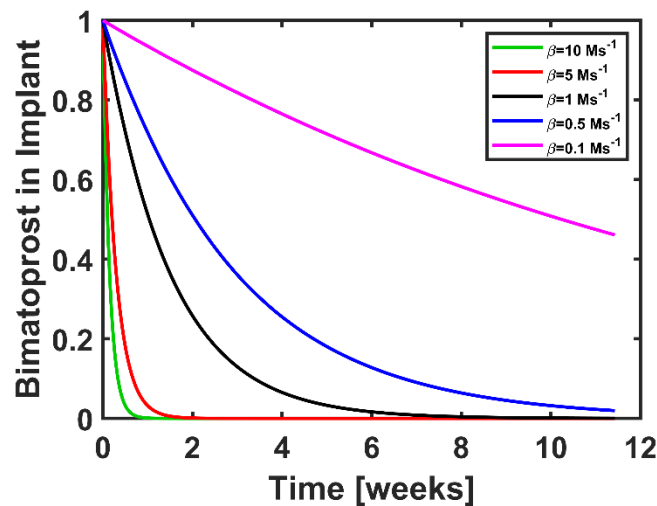


Figure 5 Time-evolution of the implant dose in the standing position. The results were normalised by the initial dose of 10 μg .

The parameter β was calibrated to attain a near-zero dose after the simulated 12 weeks. This calibration yields an approximate β value of 0.5 Ms^{-1} , which has been used to obtain the results reported in subsequent sections.

3.3. The effect of implant location on drug delivery

Figure 6 and Figure 7 show bimatoprost concentration maps in the AS for standing and supine body positions respectively. Two locations of the cylindrical implant were evaluated, including the iridocorneal angle (i.e. gravity-driven positioning mimicking Durysta[®]) and the lower part of the lens in the PC (mimicking the solution presented by SpyGlass Pharma[™]), which have been included in the plots.

The results suggest that bimatoprost tends to accumulate in the vicinity of the implant when its placement is gravity-driven in the AC (i.e., mimicking Durysta[®]), with drug concentrations $\geq 0.5 \mu\text{g/mL}$. Eddies formed by the effect of thermal convection prove not to be an effective mixing mechanism in this case. This can be visualised particularly in the snapshots corresponding to delivery time t of 3 hours, 1 week and 6 weeks in both Figure 6 (Series A) and Figure 7 (Series A). This point-source effect is observed both in the standing and the supine position and results in a highly localised delivery.

For an implant located in the PC, hence mimicking the implant developed by SpyGlass Pharma[™], there is an accumulation of bimatoprost in the vicinity of the implant, with concentrations $\geq 0.5 \mu\text{g/mL}$, but the drug is homogeneously distributed in the AC in the standing position, with concentrations that reach $\approx 0.1 \mu\text{g/mL}$ after 1 week delivery time. In the supine position however, an accumulation of drug in the vicinity of the implant is also observed, with bimatoprost concentrations $\geq 0.5 \mu\text{g/mL}$, too, while the drug is homogeneously distributed in the AC only on the side of the eye where the implant lies, with maximum concentrations $\geq 0.25 \mu\text{g/mL}$ after 1 week delivery time. This asymmetric distribution in the AC is attributed to the formation of the twin eddies observed in the analysis of the AH flow field.

It is concluded that positioning the implant next to the lens in the PC gives rise to smaller concentrations of the drug over a greater zone within the AC than positioning the implant in the iridocorneal angle in the AC. Distributing the drug over a greater volume within the AC can help with avoiding an excessively localised delivery, although it can also lead to a reduction in the drug's bioavailability in the TM due to permeation of bimatoprost into the corneal endothelium³⁶.

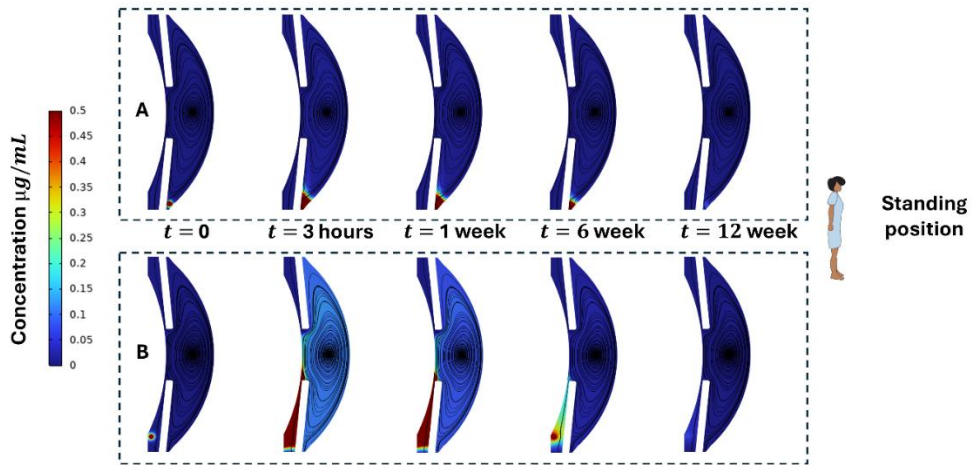


Figure 6 Vertical cross-section colour maps of the bimatoprost concentration [$\mu\text{g/mL}$] in the eye's anterior segment in the standing position at different times during the simulated 3 months' delivery. The cross-sections contain the eye centre. Series (A) shows the results for an implant located in the iridocorneal angle (Durysta[®]). Series (B) corresponds to the results obtained for a cylindrical implant located in the posterior chamber, next to the lens, mimicking SpyGlass Pharma[™] solution.

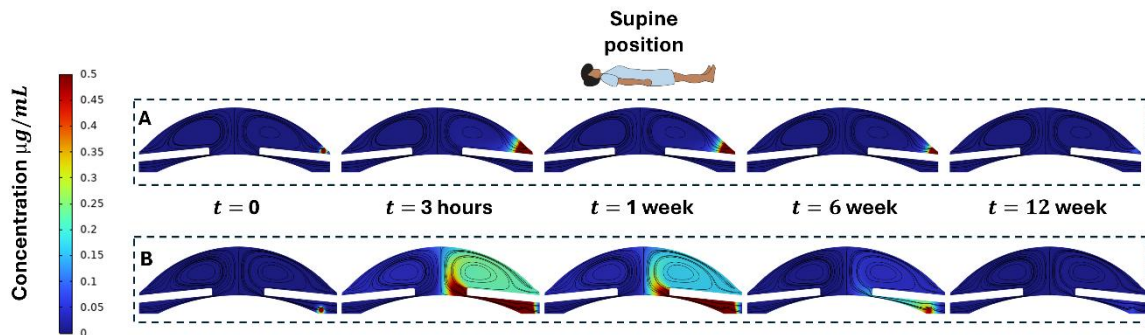


Figure 7 Cross-section maps (containing the eye's centre) of the bimatoprost concentration [$\mu\text{g/mL}$] in the eye's anterior segment in the supine position at different times during the simulated 3 months' delivery. Series (A) shows the results for the implant placed in the iridocorneal angle. Series (B) corresponds to the results obtained for a cylindrical implant located in the posterior chamber, in the vicinity of the lens.

Figure 8 shows 3-D contour plots of bimatoprost, which illustrates the extent of drug distribution in the AC after 1 week's delivery time, and confirming the results shown in the 2-D plots analysed in Figure 6 and Figure 7. Plots have been included for both the standing and supine body positions and the two implant locations, but only for delivery time $t = 1$ week. It is observed that body posture does not affect the extent of drug delivery when the implant is located by gravity in the iridocorneal angle, where the highly localised delivery (i.e., point source effect) becomes evident. When the implant is located next to the lens in the PC however, it can be seen that the drug is distributed over a greater zone than when the implant is located in the AC. It is observed, too, that the standing position gives way to a greater distribution area than the supine position. In either case, however, there are significant areas of the TM where the concentration of bimatoprost is near-zero.

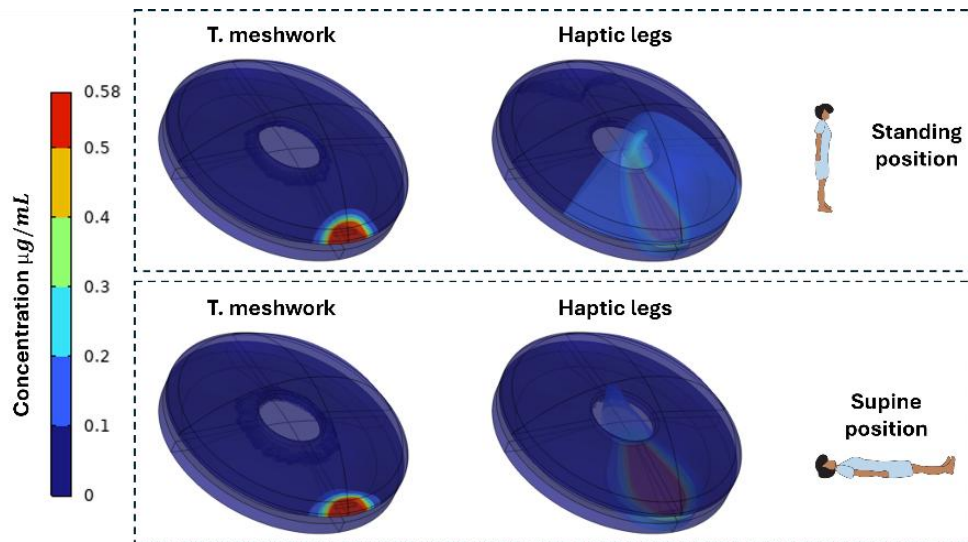


Figure 8 3-D Contour plots of bimatoprost concentration at delivery time $t = 1$ week.

The concentration profiles observed may open the door towards personalised treatment as the optimal therapeutic strategy may vary from patient to patient. Location of the implant in the iridocorneal angle gives way to highly localised drug delivery regardless of body position. It can be speculated that this strategy will be efficient when the effect of the drug in a small portion of the TM is enough to open a way for sufficient AH draining. Placing the implant next to the lens gives smaller concentrations, but the drug reaches a greater portion of the TM with respect to iridocorneal positioning. In the latter strategy, there is also a risk that bimatoprost permeating into the corneal endothelium, causing a reduction of the drug's bioavailability.

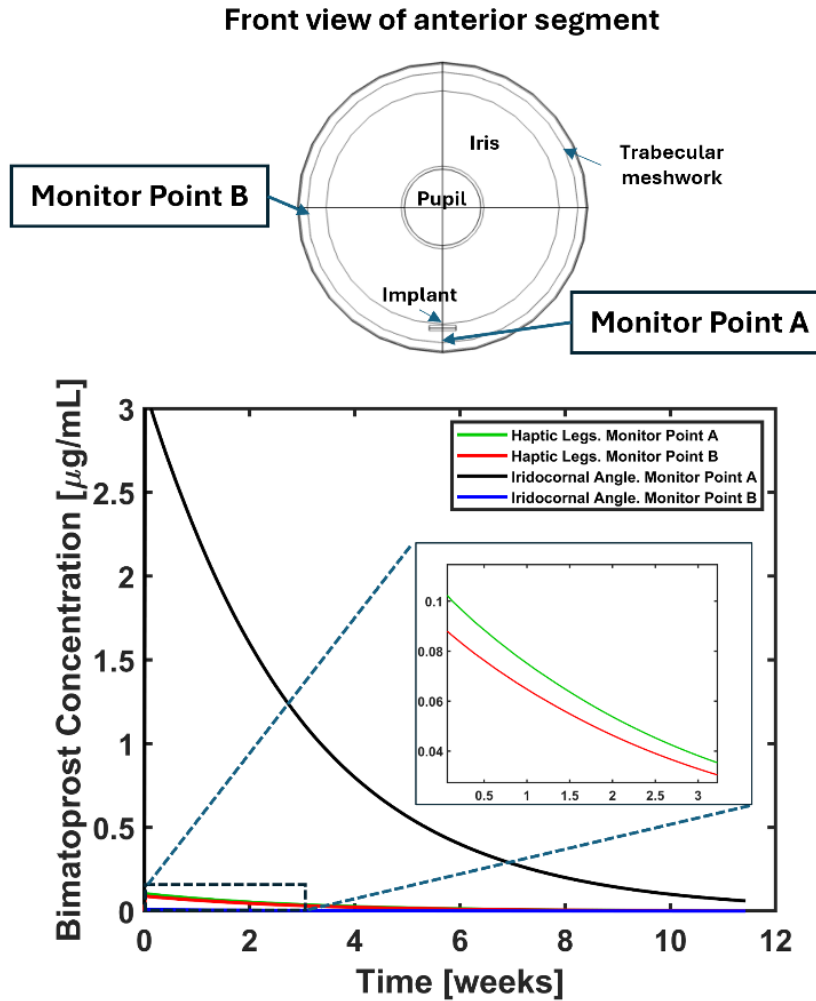


Figure 9 Time evolution of drug concentration at a monitor point in the TM during the 12 weeks' delivery time. Standing position has been considered.

Figure 9 quantifies drug delivery localisation for the standing position. Two monitor points were set up in the simulations: Monitor Point A corresponds to the boundary between the TM at the lowest part of the eye, while Monitor Point B corresponds to the side of the eye. When the cylindrical implant is placed in the TM, the concentration in the instant following the beginning of delivery is $3 \mu\text{g/mL}$ and reduces following the expected exponential trend over the 12 weeks' delivery time (*black* data series), while the concentration observed in Monitor Point B is negligible (*blue* data series). When the cylindrical implant is placed next to lens, the differences in concentration are smaller, with a value of $0.1 \mu\text{g/mL}$ in Monitor Point A (*green* data series) and $0.09 \mu\text{g/mL}$ in Monitor Point B (*red* data series).

The results suggest that an annular implant could give way to highly localised drug delivery in the entirety of the TM, with only small concentrations reaching the cornea, hence minimising permeation into the corneal endothelium. The results obtained for the hypothetical annular

implant are shown in Figure 10. The same dose of $10 \mu\text{g}$ has been implemented. The results show a temporal evolution in Monitor Point B of approximately $0.15 \mu\text{g/mL}$. Low concentrations in the TM could be improved by increasing dosage. A 360° annular implant could, however, entail practical implantation hurdles from the surgical standpoint due to geometric restrictions, as well increased shear stress in the in ocular tissue, since partially blocking the TM may cause local acceleration of the AH. The appropriate extent of the TM covered by the optimal ring segment would be determined by the AH evacuation needs of each specific patient, hence opening the door towards personalised treatment.

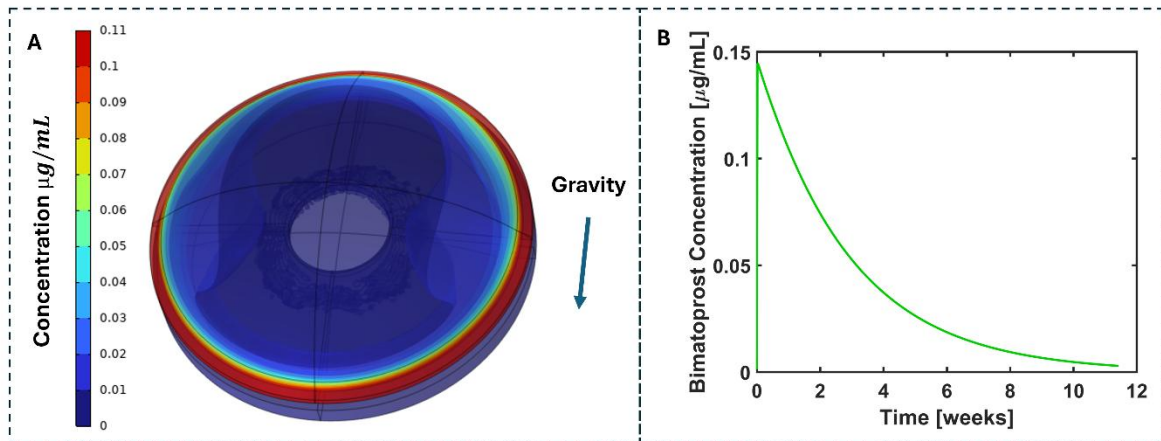


Figure 10 Concentration profiles in the AS for an annular implant (A) and evolution of the concentration at Monitor Point B during delivery time (B). The concentration profile corresponds to delivery time $t = 1$ week.

4. Conclusions

The *in-silico* study presented in this work demonstrates that the geometry and location of sustained-release intraocular implants play a decisive role in the 3-D drug distribution within the eye's AS. Our model shows that cylindrical implants placed at the iridocorneal angle or in the posterior chamber, produce markedly non-uniform concentration fields. This limitation arises because the natural convection currents generated by temperature gradients and aqueous humour flow are too weak and too directional to disperse the drug effectively throughout the AC.

Placing the implant in the PC provides improved distribution across a broader region of the AS; however, in a real scenario, this configuration may also lead to increased drug loss through the corneal endothelium, hence reducing bioavailability in the TM.. This trade-off emphasises that enhancing spatial coverage does not necessarily translate to optimal therapeutic delivery when physiological absorption pathways compete with the target site.

A theoretical annular implant was tested virtually, which delivers a substantially more homogeneous concentration profile across the trabecular meshwork. The annular geometry overcomes the inherent limitations of point-source systems, although implementing a full 360° ring implant may involve practical surgical constraints. Therefore, the results suggest that tailored partial-ring segments could still capture much of the performance benefit of the full ring while offering improved feasibility and customisation for personalised treatments.

Overall, these results highlight fundamental design principles for intraocular drug-delivery systems, in particular how implant shape and placement are critical for effective drug delivery. The insights provided in this work have the potential for guiding the next generation of ocular implants and can support both device innovation and personalised therapy optimisation for glaucoma management.

Funding

This work is supported by the Medical Research Council (grant numbers MR/T027932/1 and MR/Z504841/1).

Author contributions

U.P. conceived the simulations, performed the simulations, and post-processed results. T.C supervised the work. CY. conceived the project and supervised the work. D.S. conceived the

project, supervised the work and conceived the simulations. All authors contributed to the discussions and interpretations of the results and reviewed the manuscript.

Data availability

All relevant data and files are available upon request. Please refer to Daniel Sebastia-Saez at j.sebastiasaez@surrey.ac.uk

Competing interests statement

The authors declare no conflict of interest.

REFERENCES

1. Faiq, M. A. *et al.* A novel mathematical model of glaucoma pathogenesis. *J Curr Glaucoma Pract* **13**, 3–8 (2019).
2. Killer, H. E. & Pircher, A. What is the optimal glaucoma treatment: reducing aqueous humour production or facilitating its outflow? *Eye (Basingstoke)* vol. 34 1719–1721 Preprint at <https://doi.org/10.1038/s41433-020-0862-8> (2020).
3. Goel, M., Picciani, R. G., Lee, R. K. & Bhattacharya, S. K. *Aqueous Humor Dynamics: A Review. The Open Ophthalmology Journal* vol. 4 (2010).
4. Weinreb, R. N., Aung, T. & Medeiros, F. A. The pathophysiology and treatment of glaucoma: A review. *JAMA* vol. 311 1901–1911 Preprint at <https://doi.org/10.1001/jama.2014.3192> (2014).
5. Johnson, M., McLaren, J. W. & Overby, D. R. Unconventional aqueous humor outflow: A review. *Experimental Eye Research* vol. 158 94–111 Preprint at <https://doi.org/10.1016/j.exer.2016.01.017> (2017).
6. Wang, W., Qian, X., Song, H., Zhang, M. & Liu, Z. Fluid and structure coupling analysis of the interaction between aqueous humor and iris. *Biomed Eng Online* **15**, (2016).
7. Shan, S. *et al.* Global incidence and risk factors for glaucoma: A systematic review and metaanalysis of prospective studies. *J Glob Health* **14**, 1–14 (2024).
8. Qin, M. & Yu-Wai-Man, C. Glaucoma: Novel antifibrotic therapeutics for the trabecular meshwork. *European Journal of Pharmacology* vol. 954 Preprint at <https://doi.org/10.1016/j.ejphar.2023.175882> (2023).
9. Conlon, R., Saheb, H. & Ahmed, I. I. K. Glaucoma treatment trends: a review. *Canadian Journal of Ophthalmology* vol. 52 114–124 Preprint at <https://doi.org/10.1016/j.jcjo.2016.07.013> (2017).
10. Cursiefen, C., Cordeiro, F., Cunha-Vaz, J., Wheeler-Schilling, T. & Scholl, H. P. N. Unmet Needs in Ophthalmology: A European Vision Institute-Consensus Roadmap 2019-2025. *Ophthalmic Research* vol. 62 123–133 Preprint at <https://doi.org/10.1159/000501374> (2019).
11. Walters, T. R., Lee, S. S., Goodkin, M. L., Whitcup, S. M. & Robinson, M. R. Bimatoprost Sustained-Release Implants for Glaucoma Therapy: 6-Month Results From a Phase I/II Clinical Trial. *Am J Ophthalmol* **175**, 137–147 (2017).
12. Kesav, N. P., Capitena Young, C. E., Ertel, M. K., Seibold, L. K. & Kahook, M. Y. Sustained-release drug delivery systems for the treatment of glaucoma. *International Journal of Ophthalmology* vol. 14 148–159 Preprint at <https://doi.org/10.18240/ijo.2021.01.21> (2021).
13. Ozdemir, S., Wong, T. T., Allingham, R. R. & Finkelstein, E. A. Predicted patient demand for a new delivery system for glaucoma medicine. *Medicine (United States)* **96**, (2017).

14. Bacharach, J. *et al.* Phase 3, Randomized, 20-Month Study of the Efficacy and Safety of Bimatoprost Implant in Patients with Open-Angle Glaucoma and Ocular Hypertension (ARTEMIS 2). *Drugs* **81**, 2017–2033 (2021).
15. Medeiros, F. A. *et al.* Phase 3, Randomized, 20-Month Study of Bimatoprost Implant in Open-Angle Glaucoma and Ocular Hypertension (ARTEMIS 1). *Ophthalmology* **127**, 1627–1641 (2020).
16. Seal, J. R. *et al.* Intracameral Sustained-Release Bimatoprost Implant Delivers Bimatoprost to Target Tissues with Reduced Drug Exposure to Off-Target Tissues. *Journal of Ocular Pharmacology and Therapeutics* **35**, 50–57 (2019).
17. Sarkisian, S. R. *et al.* Travoprost Intracameral Implant for Open-Angle Glaucoma or Ocular Hypertension: 12-Month Results of a Randomized, Double-Masked Trial. *Ophthalmol Ther* **13**, 995–1014 (2024).
18. Bacharach, J. *et al.* Travoprost Intracameral Implant Demonstrates Superior IOP Lowering Versus Topical Prostaglandin Analog Monotherapy in Patients with Open-Angle Glaucoma or Ocular Hypertension. *Ophthalmol Ther* <https://doi.org/10.1007/s40123-024-00992-1> (2024) doi:10.1007/s40123-024-00992-1.
19. Weinreb, R. N. *et al.* Single Administration of Bimatoprost Implant: Effects on 24-Hour Intraocular Pressure and 1-Year Outcomes. *Ophthalmol Glaucoma* **6**, 599–608 (2023).
20. Sebastia-Saez, D., Luo, J., Qin, M., Chen, T. & Yu-Wai-Man, C. Advancing glaucoma research with multiphysics continuum mechanics modelling: Opportunities and open challenges. *Journal of the Mechanical Behavior of Biomedical Materials* vol. 173 Preprint at <https://doi.org/10.1016/j.jmbbm.2025.107240> (2026).
21. Pandey, P. K., Jain, M. & Jha, P. K. Drug Delivery from a Ring Implant Attached to Intraocular Lens: An in-silico Investigation. *J Pharm Sci* <https://doi.org/10.1016/j.xphs.2024.09.001> (2024) doi:10.1016/j.xphs.2024.09.001.
22. Ferreira, J. A., De Oliveira, P., Da Silva, P. M. & Murta, J. N. Numerical simulation of aqueous humor flow: From healthy to pathologic situations. *Appl Math Comput* **226**, 777–792 (2014).
23. Fernández-Vigo, J. I. *et al.* Computational simulation of aqueous humour dynamics in the presence of a posterior-chamber versus iris-fixed phakic intraocular lens. *PLoS One* **13**, (2018).
24. Cui, L. *et al.* Study on the correlation between iris blood flow, iris thickness and pupil diameter in the resting state and after pharmacological mydriasis in patients with diabetes mellitus. *BMC Ophthalmol* **24**, (2024).
25. Repetto, R. An analytical model of the dynamics of the liquefied vitreous induced by saccadic eye movements. *Meccanica* **41**, 101–117 (2006).
26. Dvoriashyna, M., Repetto, R. & Tweedy, J. H. Oscillatory and steady streaming flow in the anterior chamber of the moving eye. *J Fluid Mech* **863**, 904–926 (2019).
27. Pan, Z. & Ding, J. Poly(lactide-co-glycolide) porous scaffolds for tissue engineering and regenerative medicine. *Interface Focus* vol. 2 366–377 Preprint at <https://doi.org/10.1098/rsfs.2011.0123> (2012).

28. Vagiakis, I. *et al.* Bimatoprost Intracameral Implant (DuroStent®): A New Era in Glaucoma Management Through Sustained-Release Innovation. *Drug Design, Development and Therapy* vol. 19 703–714 Preprint at <https://doi.org/10.2147/DDDT.S506520> (2025).
29. Choi, E. Y. *et al.* The Effect of Bimatoprost Implant on Glaucoma Patients: An Observational Study. *J Glaucoma* **33**, 431–436 (2024).
30. Zhang, J. *et al.* Microstructure visualization of conventional outflow pathway and finite element modeling analysis of trabecular meshwork. *Biomed Eng Online* **15**, (2016).
31. Abu-Hassan, D. W., Acott, T. S. & Kelley, M. J. *The Trabecular Meshwork: A Basic Review of Form and Function*.
32. Cai, J. C., Chen, Y. L., Cao, Y. H., Babenko, A. & Chen, X. Numerical study of aqueous humor flow and iris deformation with pupillary block and the efficacy of laser peripheral iridotomy. *Clinical Biomechanics* **92**, (2022).
33. Ooi, E. H. & Ng, E. Y. K. Simulation of aqueous humor hydrodynamics in human eye heat transfer. *Comput Biol Med* **38**, 252–262 (2008).
34. King, D., McCormick, C. & McGinty, S. How Does Fluid Flow Influence Drug Release from Drug Filled Implants? *Pharm Res* **39**, 25–40 (2022).
35. Yong, H. N., Ismail, Z., Lim, Y. J. & Muna'aim, M. A. Modelling gravity-driven aqueous humour flow and drug delivery in Descemet's membrane detachment. *Alexandria Engineering Journal* **107**, 184–197 (2024).
36. Chen, W. *et al.* Corneal alterations induced by topical application of commercial latanoprost, travoprost and bimatoprost in rabbit. *PLoS One* **9**, (2014).